Check for updates

ADVANCED OPTICAL MATERIALS
www.advopticalmat.de

Designing High-Performance Sb_2S_3 Field-Effect Phototransistor with an Excellent Light-to-Dark Current Ratio for Weak Light Detection

Ruijin Hu, Aodi Zhang, Yunqing Cao, Zongguang Liu, Xiangdong Meng,* Junzhuan Wang, Shaobo Zhang,* and Linwei Yu*

To meet the growing multifunctional flexible applications, developing high-performance thin film photodetectors, especially based on burgeoning materials, such as antimony sulfide (Sb_2S_3) thin film, is an attractive topic. Although the Sb_2S_3 thin film has lots of advantages, such as high absorption coefficient, excellent stability, and earth abundance, the photodetectors built upon it, especially within a phototransistor framework, are still in a very early stage, let alone working principle, design strategy, and optimization methods. In this work, by performing a finite-element simulation, the working principle, as well as the effect of the device geometries (channel thickness/length) and the trap density, is investigated to explore a practical strategy to improve the performance of the Sb_2S_3 thin film phototransistor. Benefiting from the extremely low dark current modulated by the gate voltage, the device with a channel thickness of 400 nm and a channel length of 100 µm exhibits an outstanding light-to-dark current ratio of $> 10^6$, as well as the detectivity of 1.5×10^{13} Jones, photosensitivity of 1.2×10^6, and responsivity of 5.8×10^{-2} A W^{-1}. More importantly, an excellent weak-light-detecting ability can be obtained, even with a light intensity of 10 nW cm^{-2}. These results provide valuable guidance for fabricating high-performance Sb_2S_3 phototransistors and show great potential for integration within industrial-mature system-level devices.

1. Introduction

With the growing flexible applications demands for multifunctional and multi-scenario environments, developing and fabricating high-performance thin film photodetectors, to demonstrate excellent flexibility and mechanical stability, especially based on some emerging and up-and-coming materials, is an important and meaningful issue.[1–6] Recently, the antimony sulfide (Sb_2S_3) material has attracted much research interest, for its tunable bandgap (1.4–1.7 eV), high absorption coefficient (≈10^5 cm^{-1}), low toxicity, earth abundance, and excellent air stability.[7–10] For example, a remarkable power conversion efficiency (PCE) beyond 8% has been demonstrated, with a structure configuration of FTO/CdS/Sb_2S_3/Spiro-OMeTAD/Au, for the Sb_2S_3-based thin film solar cells.[11] Although a large part of such optoelectronic devices is used to detect various photoelectric signals, especially as wearable bio-detectors and bio-sensors, the investigation of Sb_2S_3-based photodetectors is still in a very early stage, except for some sporadic research works on the Sb_2S_3 nanowire photodetectors.[6,12,13] The Sb_2S_3 nanowires grown via chemical vapor deposition or hydrothermal methods usually have a random orientation and distribution, which is difficult to integrate into industrial-mature technology.[13–16] Thus, the Sb_2S_3 thin film, which can be fabricated by industrial-mature technology, such as magnetron sputtering, atomic layer deposition, and so on, should be a more proper candidate for the integration into large-scale fabrication for system-level optoelectronic devices.[10,17–21]

Few works have been reported on the Sb_2S_3 thin film photodetectors, except for some initial explorations utilizing either the photoconductor or the photodiode with a p-n/p-i-n heterojunction architecture.[22] For example, the Sb_2S_3/TiO_2 photodetectors have been demonstrated to have a detectivity of ≈10^{11} Jones, a dark current (I_{dark}) of ≈10^{-8} A, and a light current (I_{light}) of ≈10^{-6} A.[23] The I_{light}/I_{dark} in this work and other similar-structured devices based on the Sb_2S_3 thin film is relatively low due to a high I_{dark}, typically with a value of 10^2–10^3 under a light intensity of 1 mW cm^{-2}. However, the I_{light}/I_{dark} rapidly decreases to <10 under a light intensity of 1 µW cm^{-2} and below, which is required for neuromorphic vision sensors,[24] especially under dim light conditions. Thus, the signal-to-noise ratio is sig-

R. Hu, A. Zhang, Y. Cao, Z. Liu, X. Meng, S. Zhang
College of Physical Science and Technology/Microelectronics Industry Research Institute
Yangzhou University
Yangzhou 225002, P. R. China
E-mail: huruijin@yzu.edu.cn; mengxd@yzu.edu.cn; shaobozhang@yzu.edu.cn
J. Wang, L. Yu
School of Electronics Science and Engineering/National Laboratory of Solid-State Microstructures
Nanjing University
Nanjing 210093, P. R. China
The ORCID identification number(s) for the author(s) of this article can be found under https://doi.org/10.1002/adom.202501192

DOI: 10.1002/adom.202501192

 © 2025 Wiley-VCH GmbH

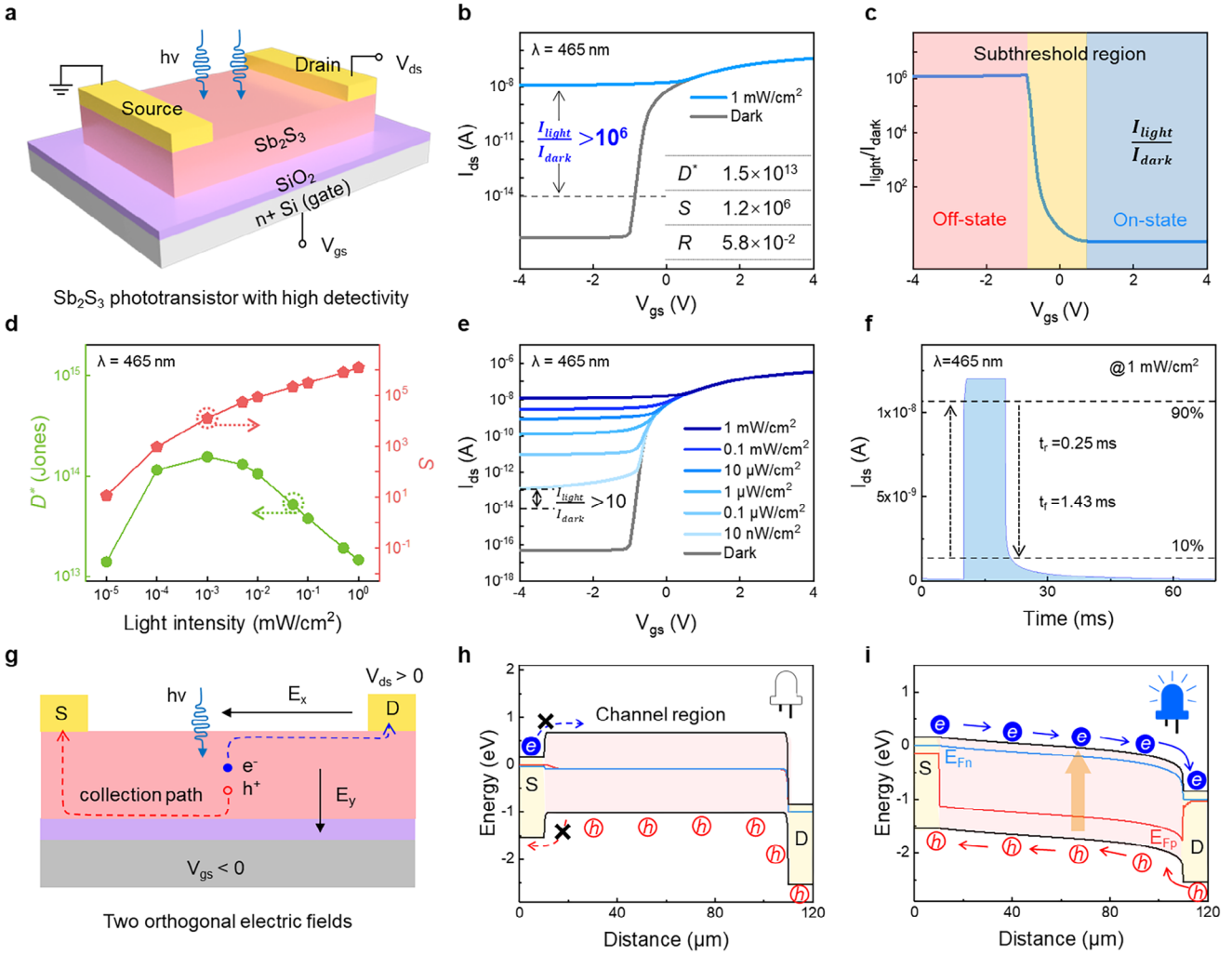


Figure 1. a) Schematic illustration of the Sb_2S_3 thin film phototransistor device with three electrodes, including source (*S*), drain (*D*), and gate (*G*). b) Transfer characteristics under dark and illumination (λ = 465 nm) conditions with detectivity (D^*), photosensitivity (*S*), and responsivity (*R*) values inserted in. Notably, the lower limit value for all simulated I_{dark} is set to 10^{-14} A in this work, when the actually calculated I_{dark} value is $<10^{-14}$ A. c) Modulation of gate voltage (V_{gs}) on the I_{light}/I_{dark} values when drain voltage (V_{ds}) holds to be 1 V. d) D^* and S values versus light intensity. (e) I_{ds}-V_{gs} curves under various light intensities. f) Transient response with rise time (t_r) and fall time (t_f) marked in it. g) Separation and collection path of photo-generated electron-hole pairs (e^--h^+) in the Sb_2S_3 channel under two orthogonal electric fields: E_x arose due to the application of V_{ds}, and E_y originated from V_{gs}. h,i) Energy band diagrams under dark and illumination conditions, respectively.

nificantly reduced, posing challenges for subsequent signal processing for weak light detection.[23,25]

To this end, the phototransistor structure, as illustrated in **Figure** 1a, can offer great advantages to modulate the carrier concentration in the channel by using a gate electrode, and thus can get an extremely low I_{dark}.[26] For example, the Sb_2S_3-based double-layer phototransistor achieves an I_{dark} of $\approx 10^{-11}$ A and an I_{light}/I_{dark} of $\approx 10^6$.[27] Furthermore, the phototransistor structure is more convenient to integrate with the well-developed complementary metal-oxide-semiconductor (CMOS) circuits, which can pave the way for implementing advanced detecting and imaging systems.[28] Although it can offer such advantages, the phototransistors built upon the Sb_2S_3 thin film lack a systematic assessment/investigation of the photodetection capabilities, and working principle, especially the influence of the gate voltage modulation, let alone design strategies for better performance.

Herein, we performed a finite-element simulation, built on a back-gate top-contact phototransistor configuration, as shown in Figure 1a, to comprehensively investigate the fundamental working mechanism, and the effect of the device geometry parameters (channel thickness/length), as well as the trap density, on the photodetection capabilities, to explore a practical and instructive designing/improving strategy for fabricating high-performance Sb_2S_3 thin film phototransistor. With an optimum channel thickness of 400 nm and channel length of 100 μm, a high I_{light}/I_{dark} > 10^6 can be gained, with a detectivity of 1.5×10^{13} Jones, photosensitivity of 1.2×10^6, and responsivity of 5.8×10^{-2} A W^{-1}, because of an extremely low I_{dark} of 10^{-14} A modulated by the gate voltage. More importantly, as channel length decreases down to

© 2025 Wiley-VCH GmbH

21951071, 2025, 22, Downloaded from https://advanced.onlinelibrary.wiley.com/doi/10.1002/adom.202501192 by Nanjing University, Wiley Online Library on [04/11/2026]. See the Terms and Conditions (https://onlinelibrary.wiley.com/terms-and-conditions) on Wiley Online Library for rules of use; OA articles are governed by the applicable Creative Commons License

2 µm, the I_{light}/I_{dark} and D^* can be improved to ≈10^7 and ≈10^{15} Jones, respectively, which shows the benefits of the scaling of Sb_2S_3 phototransistors.

2. Device Structure and Physical Model

Figure 1a schematically depicts the device structure of the Sb_2S_3 thin film phototransistor for finite-element simulation. The source/drain electrodes placed on top of Sb_2S_3 are set to be in Ohmic contact with the channel and the SiO_2 dielectric layer with a thickness of 50 nm and a highly doped silicon gate are stacked underneath the Sb_2S_3 channel, constructing a typical back-gate top-contact field-effect transistor (FET) configuration to ensure the direct illumination onto the Sb_2S_3 light absorption/channel layer. The channel thickness and length of the Sb_2S_3 phototransistor are referred to as $t_{Sb_2S_3}$ and L_{ch}, which vary from 100 to 600 nm and 0.2 to 100 µm, respectively. Two biases are applied to the device during working, one to the drain electrode (V_{ds}) and the other to the gate electrode (V_{gs}). The source electrode is connected to the ground. The refractive index (n) and extinction coefficient (k) values of the Sb_2S_3 film, extracted from the previous research,[29] are plotted in Figure S1 (Supporting Information). The material properties of the Sb_2S_3, including bandgap (E_g), electron affinity (χ), permittivity (ϵ_r), conduction band effective density of state (N_c), valence band effective density of state (N_v), doping concentration (N_D), electron mobility (μ_e) and hole mobility (μ_h) are defined in the model and listed in Table S1 (Supporting Information).[30–32]

The electrical characteristics of the device are predicted by numerically solving coupled equations including Poisson's equation, the continuity equations, and the drift-diffusion transport equations for electrons and holes by using the finite element method:

$$\mathrm{div}(\varepsilon\nabla\psi) = -\rho \tag{1}$$

$$\frac{\partial n}{\partial t} = \frac{1}{q}div\overrightarrow{J_n} + G_n - R_n \tag{2}$$

$$\frac{\partial p}{\partial t} = \frac{1}{q}div\overrightarrow{J_p} + G_p - R_p \tag{3}$$

$$\overrightarrow{J_n} = qn\mu_n\overrightarrow{E_n} + qD_n\nabla n \tag{4}$$

$$\overrightarrow{J_p} = qp\mu_p\overrightarrow{E_p} - qD_p\nabla p \tag{5}$$

where ψ is the electrostatic potential, ϵ is the local permittivity, ρ is the local space charge density, n and p are the electron and hole concentration, $\overrightarrow{J_n}$ and $\overrightarrow{J_p}$ are the electron and hole current densities, G_n and G_p are the generation rates for electrons and holes, R_n and R_p are the recombination rates for electrons and holes, q is the magnitude of the charge on an electron, μ_n and μ_p are the electron and hole mobilities, $\overrightarrow{E_n}$ and $\overrightarrow{E_p}$ are the effective electric fields for electrons and holes, and D_n and D_p are the diffusion coefficients of the electrons and holes.

For the device under illumination, the optical intensity profiles are calculated and then converted into photogeneration rates, which are integrated into the generation terms in the continuity equations. The optical intensity at each mesh point is determined by tracing the path of light from the source to the point, where the refractive index is used to calculate the reflection and transmission rates of light. The light absorption and photogeneration rates are assessed by the extinction coefficient:

$$G_{abs} = \eta_0 \frac{P\lambda}{hc}\alpha e^{-\alpha\gamma} \tag{6}$$

where η_0 is the internal quantum efficiency, which represents the number of electron-hole pairs generated per photon, P is the ray intensity factor including the effect of reflections, transmissions, and absorptions, λ is the wavelength, h is Planck's constant, c is the speed of light, α is the absorption coefficient given by $\alpha = \frac{4\pi}{\lambda}k$.

The Shockey-Read-Hall (SRH) recombination rate is determined by:

$$R_{SRH} = \frac{pn - n_i^2}{\tau_{n0}[n + n_i e(\frac{E_{trap}}{kT})] + \tau_{p0}[p + n_i e(\frac{-E_{trap}}{kT})]} \tag{7}$$

where E_{trap} is the difference between the trap energy level and the intrinsic Fermi level E_i, τ_{n0}, and τ_{p0} are the electron and hole lifetimes, n_i is the intrinsic carrier concentration, and T is the temperature.

Gaussian-distributed donor-like bulk defects are incorporated into the Sb_2S_3 thin film to analyze their influence on photodetection performance. The detailed parameters of the defects, including the peak trap energy, the capture cross-section, and characteristic decay energy, are provided in Table S2 (Supporting Information).

The performance of the phototransistor is evaluated based on the photosensitivity (S), responsivity (R), and detectivity (D^*):

$$S = \frac{I_{light} - I_{dark}}{I_{dark}} \tag{8}$$

$$R = \frac{I_{light} - I_{dark}}{P_{in}A} \tag{9}$$

$$D^* = R\sqrt{\frac{A}{2qI_{dark}}} \tag{10}$$

where I_{dark} and I_{light} are the I_{ds} under dark and illumination conditions, P is the light intensity, A is the effective area.

3. Results and Discussion

Figure 1b shows the typical transfer curves (I_{ds}-V_{gs}) of the Sb_2S_3 thin film phototransistor under dark and illumination conditions, with an outstanding I_{light}/I_{dark} value of ~10^6, as well as an excellent D^* of 1.5×10^{13} Jones, S of 1.2×10^6, and R of 5.8×10^{-2} A W^{-1}. Taking notice, according to the lower limit of the measuring instrument (~10^{-14} A), all the simulated I_{dark} is set to 10^{-14} A in this work, when the actually calculated I_{dark} is below 10^{-14} A, as indicated by the grey dashed line in Figure 1b. The Sb_2S_3 phototransistor significantly outperforms its photoresistor

© 2025 Wiley-VCH GmbH

21951071, 2025, 22, Downloaded from https://advanced.onlinelibrary.wiley.com/doi/10.1002/adom.202501192 by Nanjing University, Wiley Online Library on [04/11/2026]. See the Terms and Conditions (https://onlinelibrary.wiley.com/terms-and-conditions) on Wiley Online Library for rules of use; OA articles are governed by the applicable Creative Commons License

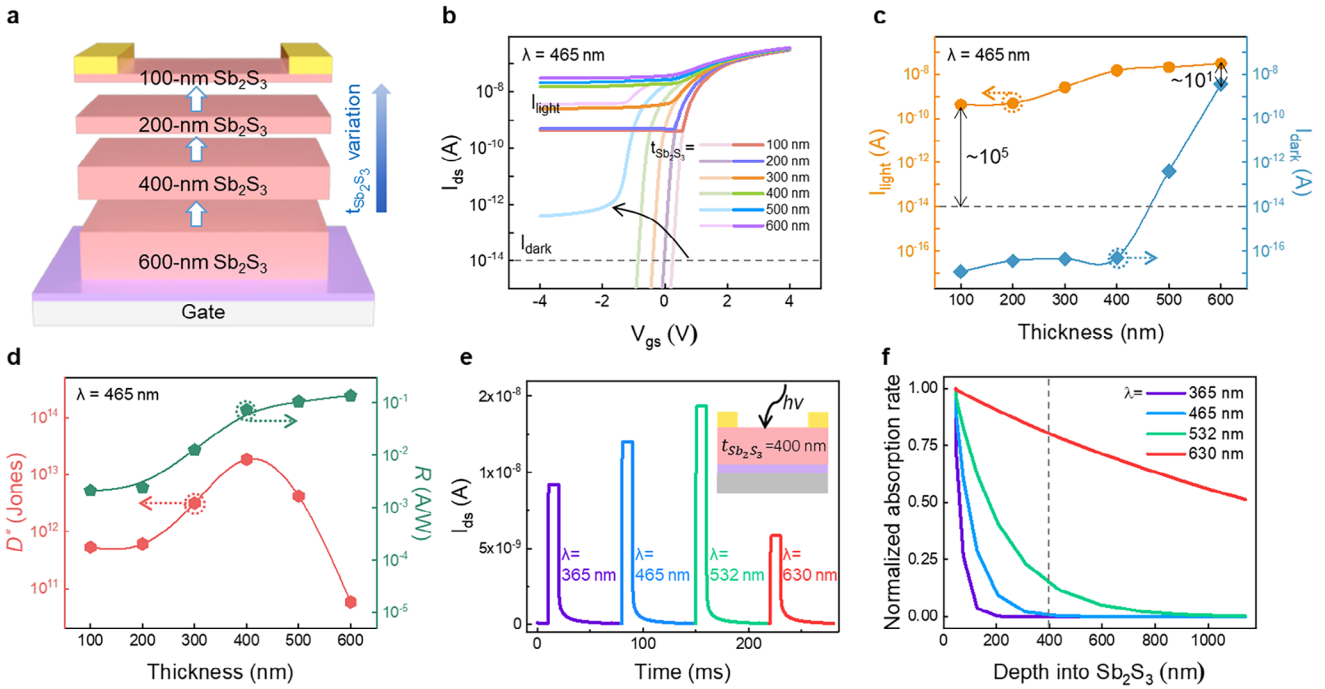


Figure 2. a) Schematic of the Sb_2S_3 thin film phototransistors with channel thicknesses ($t_{Sb_2S_3}$) varied from 100 to 600 nm, while the channel length is fixed at 100 μm. b) Simulated I_{ds}-V_{gs} curves of the devices under dark and light illumination, and c) extracted I_{light} and I_{dark} values, as well as d) simulated D^* and R values, under the $\lambda = 465$ nm. e) Time response diagrams of the phototransistor with a channel thickness of 400 nm. f) Normalized absorption rate as a function of depth into the Sb_2S_3 channel under different wavelengths.

and photodiode counterparts, as demonstrated in Figure S2 (Supporting Information). More interestingly, as seen in Figure 1c, the I_{light}/I_{dark} for the Sb_2S_3 thin film phototransistors can be greatly modulated by the V_{gs}, which can be divided into three regions (on-state, subthreshold, off-state). In the on-state region ($V_{gs} > 1$ V), I_{dark} has almost the same value as I_{light}, with an I_{light}/I_{dark} value of ≈1. This is because the intrinsic carrier concentration in the channel is already sufficiently high under dark conditions, exposing the device to light causes only a slight increase in the current. In the subthreshold region (-1 V< V_{gs} < 1 V), an almost unchanged or slightly increasing I_{light}, but an obviously and rapidly decreasing I_{dark} are presented, resulting in a sudden increase of the I_{light}/I_{dark}. In comparison, in the off-state regime ($V_{gs} < -1$ V), the applied V_{gs} fully depletes the carriers in the channel, suppressing I_{dark} to an ultralow level (<10^{-14} A). Under illumination, the photo-generated carrier concentration substantially exceeds the original value in the depleted channel, leading to a significant increase in current. As a result, the highest I_{light}/I_{dark}, as well as the D^*, can be achieved for the n-type Sb_2S_3 thin film transistor in the off-state region (pink zone), as shown in Figure 1c and Figure S3 (Supporting Information). Thus, further simulations under different incident light intensities (λ = 465 nm, from 10^{-5} to 1 mW cm^{-2}) have been carried out to investigate the weak-light-detecting capability of such V_{gs}-modulated devices, and the obtained I_{ds}-V_{gs} curves are shown in Figure 1e, as well as the extracted corresponding values of D^*, S and R in Figure 1d and Figure S4 (Supporting Information). With the increasing light intensity, ranging from 10^{-5} to 1 mW cm^{-2}, the D^* first increases slightly, and then decreases, with a maximum value of ≈10^{14} Jones at 1 μW cm^{-2}, and a minimum value beyond 10^{13} Jones even with a light intensity of 10 nW cm^{-2}, which indeed reveals an excellent weak-light-detecting capability of such V_{gs}-modulated Sb_2S_3 thin film transistor. Also, the ideal Sb_2S_3 phototransistor has a rise time (τ_r) of 0.25 ms and a fall time (τ_f) of 1.43 ms by setting the value of the electron mobility at 0.8 cm^2 Vs^{-1}.

Unlike the p-n photodiodes with only a vertical electric field, the Sb_2S_3 phototransistors feature two orthogonal electric fields, a horizontal electric field (E_x) and a vertical electric field (E_y), as illustrated in Figure 1g. The E_x is determined by V_{ds} and L_{ch}, while E_y can be adjusted by V_{gs} and the thickness of the SiO_2 layer. Under illumination ($h\nu \geq E_g$), the electron-hole pairs can be generated in the Sb_2S_3 channel, and then separated by the electric fields. Under E_y, the photo-generated electrons will move upward, and then drift to the drain with the assistance of E_x, as indicated by the blue dashed line in Figure 1g. Considering the finite lifetime of photo-generated carriers (18 ns) and the long channel length (100 μm), only electrons near the drain can be effectively collected. As for the holes, most of them are attracted to the bottom of the channel, with little chance of being collected. Figure 1h,i demonstrate the band diagrams at the surface of the Sb_2S_3 channel with V_{gs} of -3 V and V_{ds} of 1 V. At dark, the thin film enables the full depletion of the channel, thus blocking the transportation of the carrier. As a result, the device exhibits an extremely low dark current. Under illumination, as shown in Figure 1i, the large photo-generated electron-hole pairs can lower the barrier to enable movement. These results provide a promising approach and reasonable design to enable an excellent weak light detection capability of the Sb_2S_3 thin film transistor.

© 2025 Wiley-VCH GmbH

21951071, 2025, 22, Downloaded from https://advanced.onlinelibrary.wiley.com/doi/10.1002/adom.202501192 by Nanjing University, Wiley Online Library on [04/11/2026]. See the Terms and Conditions (https://onlinelibrary.wiley.com/terms-and-conditions) on Wiley Online Library for rules of use; OA articles are governed by the applicable Creative Commons License

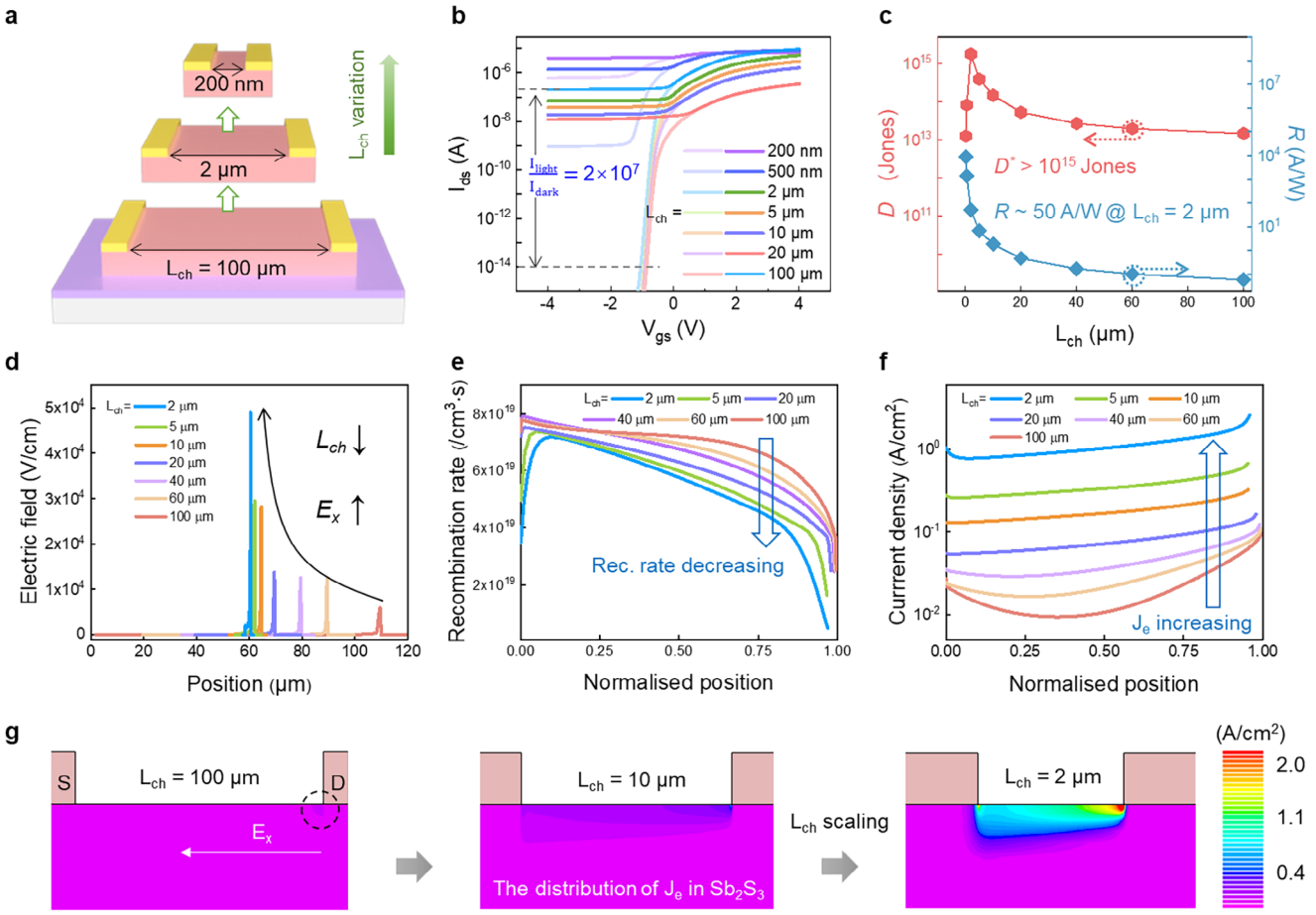


Figure 3. a) Illustration of the phototransistors with the channel length (L_{ch}) varied from 100 μm to 200 nm, while the channel thickness is fixed at 400 nm. b) Transfer characteristics of Sb_2S_3 devices, where the I_{light}/I_{dark} can achieve a value of 2×10^7 with $L_{ch} = 2$ μm. c) D^* and R of devices with different L_{ch} values. d–f) Evolution of the E_x, recombination rate, and electron current density (J_e) with respect to L_{ch}, respectively. g) Simulated J_e distribution for the Sb_2S_3 channel.

As shown in **Figure** 2a, a simulation was performed on different Sb_2S_3 channel/absorber thicknesses ($t_{Sb_2S_3}$) ranging from 100 to 600 nm, to seek a preferable $t_{Sb_2S_3}$, which will allow a reasonable balance between sufficient incident light absorption (a large enough I_{light}) and the gate control capability (a small enough I_{dark}) for better photo-sensing performance. Figure 2b shows the I_{ds}–V_{gs} curves simulated under dark and 1 mW cm^{-2} illumination ($\lambda = 465$ nm) conditions. It can be seen that with the increasing $t_{Sb_2S_3}$, the I_{light} shows a monotonically increasing trend with a ≈2 orders of magnitude increase. As to I_{dark}, as shown in Figure 2c, it remains a rather low value of $<10^{-14}$ A when $t_{Sb_2S_3} \leq 400$ nm, but when $t_{Sb_2S_3} > 400$ nm, it shows a strikingly rapid increase up to $\approx 10^{-9}$ A at $t_{Sb_2S_3} = 600$ nm, which can be attributed to the decreasing V_{gs} modulation caused by a too thick channel, resulting in a lower I_{light}/I_{dark} value. Also, the calculated D^*, R, and S values are plotted as a function of $t_{Sb_2S_3}$ in Figure 2d and Figure S5 (Supporting Information). It is interesting to find that the R increases monotonically, while the D^* and S increase first and reach their maximum value at $t_{Sb_2S_3} = 400$ nm, and then decrease.

Furthermore, the static and dynamic responses to light with different wavelengths, ranging from 365 to 630 nm, are calculated to gain a deep insight into the photo-sensing capability of the Sb_2S_3 transistor. The transfer curves under light illumination ($\lambda = 365$, 532, and 630 nm), as well as the calculated D^*, S, and R values, are shown in Figure S6 (Supporting Information). When $t_{Sb_2S_3} = 400$ nm, the highest I_{light} value, as well as the corresponding I_{light}/I_{dark} of 1.4×10^6, can be obtained for $\lambda = 532$ nm (green light) with a light intensity of 1 mW cm^{-2}, while the lowest I_{light} value and I_{light}/I_{dark} of 5.8×10^5 for $\lambda = 630$ nm (red light), which can be attributed to the too thin absorber thickness. Ideally, one absorbed photon ($h\nu > E_g$) generates one electron-hole pair in the Sb_2S_3 channel, thus the electron-hole pair generation rate (G) is numerically equal to the absorption rate (*Abs.*). Therefore, as shown in Figure 2f and Figure S7 (Supporting Information), for high-energy light, such thickness ($t_{Sb_2S_3} = 400$ nm) can absorb the whole photons ($h\nu_{365\,nm} > h\nu_{532\,nm}$, thus the number of photons of 532 nm light is more than that of 365 nm under the same light intensity), while for low-energy light, such as $\lambda = 630$ nm (red light), only a partial absorption happens. As a result, the I_{light} for 630 nm is smaller than the others. Even though a thicker Sb_2S_3 film will benefit the photon absorption of the light at long wavelengths, it comes at the expense of the gate control capability.

The L_{ch} is another critical factor in regulating the photodetecting capabilities. As shown in **Figure** 3a, the simulation

© 2025 Wiley-VCH GmbH

21951071, 2025, 22, Downloaded from https://advanced.onlinelibrary.wiley.com/doi/10.1002/adom.202501192 by Nanjing University, Wiley Online Library on [04/11/2026]. See the Terms and Conditions (https://onlinelibrary.wiley.com/terms-and-conditions) on Wiley Online Library for rules of use; OA articles are governed by the applicable Creative Commons License

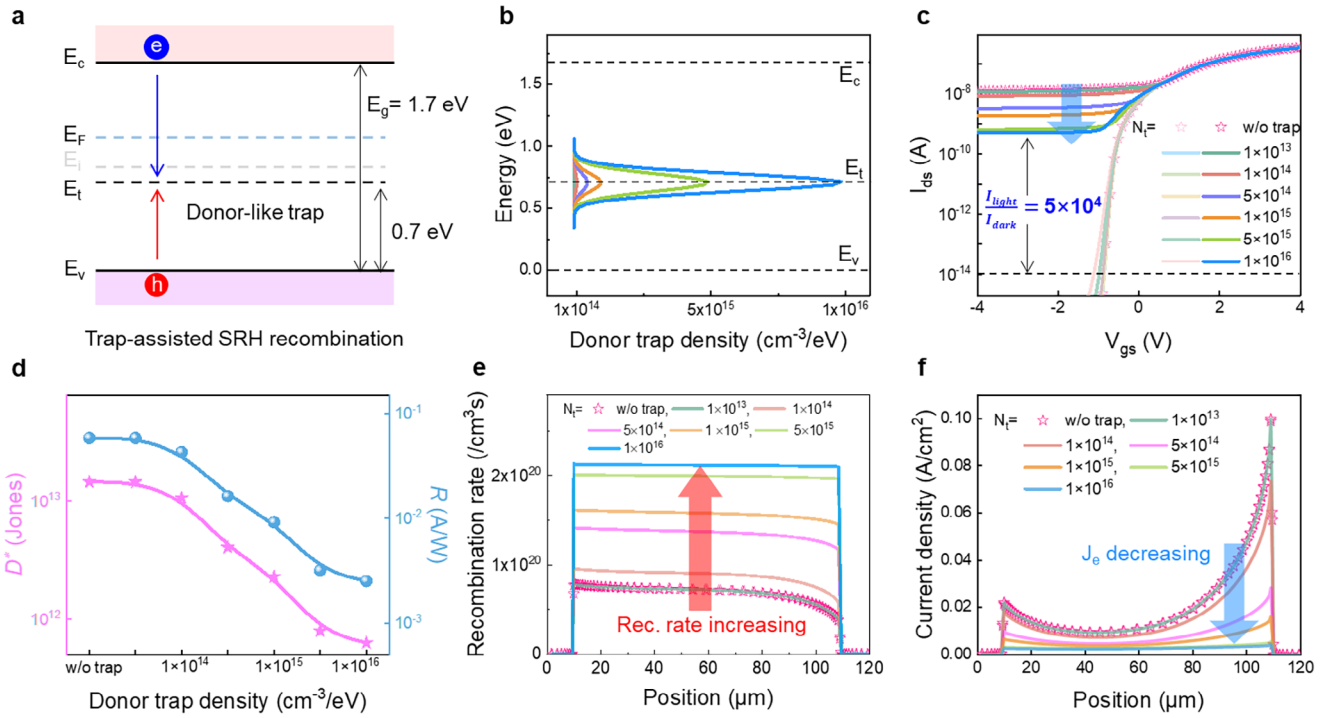


Figure 4. a) Schematic diagram of the recombination process for the phototransistor with deep-level traps. b) Trap energy level distribution with different trap densities (N_t) in the Sb_2S_3 channels. c) I_{ds}–V_{gs} curves of devices with different N_t, where the channel thickness and length are 400 nm and 100 μm, respectively. d) D^* and R as a function of the trap densities. e,f) Recombination rate and J_e along the channel direction.

model of the Sb_2S_3 phototransistors, with different L_{ch} values increasing from 0.2 to 100 μm, is built and carried out, as well as the calculated I_{ds}-V_{gs} under illumination (λ = 465 nm) in Figure 3b, which shows a decreasing trend of I_{light}/I_{dark} with increasing L_{ch}, achieving an impressive value of 2×10^7 at L_{ch} = 2 μm. However, the further reduction of L_{ch} <2 μm can lead to inefficient gate control ability, causing an increase in the dark current, which results in the degradation of the photo-sensing performance, as demonstrated in Figure 3c, Figures S8, and S9 (Supporting Information). The D^* and S achieve their highest values, D^* of > 10^{15} Jones and S of 2×10^7 at L_{ch} = 2 μm, while R is 50 A W^{-1}. Such varied trends can be attributed to the L_{ch}-induced E_x variations. With a fixed V_{ds}, the E_x significantly increases, as the L_{ch} decreases, as shown in Figure 3d, which results in a much shorter transit time and a lower recombination rate for the photo-generated carriers (Figure 3e). Furthermore, the photo-generated electron current densities (J_e) along the channel direction near the surface of the Sb_2S_3 channel are simulated and shown in Figure 3f, which can directly decide the I_{light}. When the L_{ch} = 100 μm, only the electrons near the drain electrode can be collected, and others cannot be efficiently collected because the electrons are recombined during the moving process, in other words, the transit time is larger than its lifetime. As to L_{ch} = 2 μm, the shorter channel ensures a shorter transit time, which enables the effective collection of photo-generated electrons away from the drain electrode and achieves higher J_e and I_{light} values. As shown in Figure 3f, the J_e can be effectively modulated by the L_{ch}, especially under the L_{ch}<20 μm. Besides, given that I_{dark} remains <10^{-14} A (the lower limit is set to10^{-14} A), even for the device with L_{ch} of 2 μm, an enhanced D^* can be expected/designed for the scaled devices, which shows a promising potential to integrate a high-density Sb_2S_3 phototransistor array into an advanced neuromorphic vision system.

In the actually deposited Sb_2S_3 thin film, the bulk traps, especially the deep-level traps, are inevitable, regardless of the fabrication methods. Thus, for a deeper insight into the practical applications, donor-like traps in a Gaussian distribution are implemented into the Sb_2S_3 channel, which will result in the trap-assisted SRH recombination process, reducing the lifetime of photo-generated carriers and I_{light}. As shown in **Figure** 4a, the peak of Gaussian distributed traps is located at 0.7 eV above the valence band, as well as other detailed parameters including the capture cross-sections in Table S2 (Supporting Information).[10,33] As shown in Figure 4b, the simulation was carried out to investigate the effect of the trap density (N_t) varying from 1×10^{13} to 1×10^{16} cm^{-3} eV^{-1} on the photo-detecting capabilities of devices. When under $N_t = 1 \times 10^{16}$ cm^{-3} eV^{-1}, the I_{light}/I_{dark} decreases almost 2 orders of magnitude to the value of 5×10^4, compared to the ideal device without traps (Figure 4c). Interestingly, the performance of Sb_2S_3 phototransistors, such as the D^*, R, and S, is nearly kept constant when the trap density <1×10^{14} cm^{-3} eV^{-1}, as presented in Figure 4d and Figure S10 (Supporting Information). While the N_t is raised beyond this critical value, the performance rapidly declines. Figure 4e plots the extracted recombination rate along the channel direction. As expected, the recombination rate climbs dramatically with the growth of N_t, resulting in easier recombination of the photo-generated carriers before being efficiently collected, which is consistent with the simulated J_e distribution in Figure 4f and Figure S11 (Supporting Information), where only a limited J_e is generated under illumination for

© 2025 Wiley-VCH GmbH

21951071, 2025, 22, Downloaded from https://advanced.onlinelibrary.wiley.com/doi/10.1002/adom.202501192 by Nanjing University, Wiley Online Library on [04/11/2026]. See the Terms and Conditions (https://onlinelibrary.wiley.com/terms-and-conditions) on Wiley Online Library for rules of use; OA articles are governed by the applicable Creative Commons License

devices with high trap density. These results show that the trap density in the thin film should be kept below 1×10^{14} cm^{-3} eV^{-1} to ensure the high performance of Sb_2S_3 phototransistors.

4. Conclusion

In summary, we have performed a finite-element simulation with a back-gate top-contact transistor configuration to explore a practical strategy for fabricating Sb_2S_3 thin film photodetectors with excellent weak light detection capability. Benefitting from the high absorption coefficient of Sb_2S_3 to enable the high light current and the gate voltage modulation to achieve extremely low dark current, a high light-to-dark current ratio of $\approx 10^6$, as well as the decent detection of light with intensity down to 10 nW cm^{-2}, have been achieved for a device with 100 µm channel length. The proposed Sb_2S_3 phototransistor significantly outperforms its photoresistor and photodiode counterparts, which usually have a limited light-to-dark current ratio of ≈10 and $\approx 10^3$, respectively. Our results reveal that the device geometry, including the channel thickness and channel length, needs to be carefully designed to derive the ideal photo-detecting performance. These results obtained from the thicker Sb_2S_3 film and short channel length are advantageous for light current but can increase dark current due to the degradation of gate control ability. For example, the Sb_2S_3 phototransistor with a thickness of 400 nm and a channel length of 2 µm demonstrates an enhanced light-to-dark current ratio of 2×10^7, a detectivity of $\approx 10^{15}$ Jones, and a responsitivity of ≈50 A W^{-1}. Moreover, to guide the experimental presentation of the Sb_2S_3 transistor, the influence of bulk trap density is also investigated, revealing that a trap density lower than 1×10^{14} cm^{-3} eV^{-1} has a negligible effect on the performance, while a trap density of 1×10^{16} cm^{-3} eV^{-1} would reduce the light-to-dark current ratio down to 5×10^4. These results highlight the promising potential for constructing high-performance Sb_2S_3 phototransistors, which are widely applicable to the neuromorphic vision system, bio-signal detection, and image sensors.

Supporting Information

Supporting Information is available from the Wiley Online Library or from the author.

Acknowledgements

The authors acknowledged the financial support from the National Natural Science Foundation of China under No. 62304200, 62404196, and 61974064, Natural Science Foundation of Jiangsu Province under No. BK20230562, Innovation Technology platform project jointly built by Yangzhou City and Yangzhou University under No. YZ2020268, National Natural Science Foundation of China for Distinguished Young Scholars under No. 62325403, and National Key Research Program of China under No. 92164201.

Conflict of Interest

The authors declare no conflict of interest.

Data Availability Statement

The data that support the findings of this study are available from the corresponding authors upon reasonable request.

Keywords

numerical simulation, phototransistor, Sb_2S_3 thin film, weak light detection

Received: April 15, 2025
Revised: May 13, 2025
Published online: June 14, 2025

[1] C. M. Lochner, Y. Khan, A. Pierre, A. C. Arias, *Nat. Commun.* **2014**, *5*, 5745.
[2] W. Wu, X. Wang, X. Han, Z. Yang, G. Gao, Y. Zhang, J. Hu, Y. Tan, A. Pan, C. Pan, *Adv. Mater.* **2019**, *31*, 1805913.
[3] J. Yang, M. Chen, G. Chen, Y. Hou, Z. Su, S. Chen, J. Zhao, G. Liang, *Adv. Sci.* **2024**, *11*, 2310193.
[4] K. Leng, I. Abdelwahab, I. Verzhbitskiy, M. Telychko, L. Chu, W. Fu, X. Chi, N. Guo, Z. Chen, Z. Chen, C. Zhang, Q. H. Xu, J. Lu, M. Chhowalla, G. Eda, K. P. Loh, *Nat. Mater.* **2018**, *17*, 908.
[5] S. Zhang, C. Chen, Y. Cao, X. Meng, R. Hu, Z. Liu, H. Gao, X. Jiang, J. Wang, L. Yu, *J. Phys. Chem. Lett.* **2024**, *15*, 9548.
[6] Y. Ma, C. Ma, H. Yi, H. Liang, W. Wang, Z. Zheng, Y. Zou, Z. Deng, J. Yao, G. Yang, *Adv. Opt. Mater.* **2024**, *12*, 2302039.
[7] G. Li, J. Dong, P. Xiao, B. Che, Y. Huang, Y. Zhang, R. Tang, C. Zhu, T. Chen, *Sci. China Mater.* **2022**, *65*, 3411.
[8] R. Kondrotas, C. Chen, J. Tang, *Joule* **2018**, *2*, 857.
[9] U. A. Shah, S. Chen, G. M. G. Khalaf, Z. Jin, H. Song, *Adv. Funct. Mater.* **2021**, *31*, 2100265.
[10] J. Chen, G. Li, Z. Xu, C. Xu, F. Naveed, B. Liu, Y. Zhang, R. Zhou, C. Chen, M. Wang, J. Xu, L. Li, *Adv. Funct. Mater.* **2024**, *34*, 2313676.
[11] H. Deng, X. Feng, Q. Zhu, Y. Liu, G. Wang, C. Zhang, Q. Zheng, J. Wu, W. Wang, S. Cheng, *Sci. China Mater.* **2024**, *67*, 3666.
[12] S. Fu, X. Liu, H. Dou, R. Ali, A. Zeng, J. Man, X. Zheng, H.-E. Wang, *J. Mater. Chem. A* **2024**, *12*, 28012.
[13] K. Ye, B. Wang, A. Nie, K. Zhai, F. Wen, C. Mu, Z. Zhao, J. Xiang, Y. Tian, Z. Liu, *J. Mater. Sci. Technol.* **2021**, *75*, 14.
[14] H. Bao, X. Cui, C. M. Li, Q. Song, Z. Lu, J. Guo, *J. Phys. Chem. C* **2007**, *111*, 17131.
[15] Q. Han, S. Sun, D. Sun, J. Zhu, X. Wang, *RSC Adv.* **2011**, *1*, 1364.
[16] H. Zhang, C. Hu, Y. Ding, Y. Lin, *J. Alloys Compd.* **2015**, *625*, 90.
[17] C. Gao, J. Huang, H. Li, K. Sun, Y. Lai, M. Jia, L. Jiang, F. Liu, *Ceram. Int.* **2019**, *45*, 3044.
[18] H. Li, G. Q. Yang, X. Y. Hu, Y. H. Hu, R. B. Zeng, J. R. Cai, L. Q. Yao, L. M. Lin, L. P. Cai, G. Chen, *Adv. Sci.* **2023**, *10*, 2303414.
[19] Z. Wang, G.-J. Chen, R. Tang, Z.-H. Su, C.-Y. Duan, S.-M. Chen, Y.-L. Sun, S. Chen, G.-X. Liang, *Ceram. Int.* **2024**, *50*, 4729.
[20] P. Büttner, F. Scheler, C. Pointer, D. Döhler, M. K. S. Barr, A. Koroleva, D. Pankin, R. Hatada, S. Flege, A. Manshina, E. R. Young, I. Mínguez-Bacho, J. Bachmann, *ACS Appl. Energy Mater.* **2019**, *2*, 8747.
[21] S.-J. Lee, S.-J. Sung, K.-J. Yang, J.-K. Kang, J. Y. Kim, Y. S. Do, D.-H. Kim, *ACS Appl. Energy Mater.* **2020**, *3*, 12644.
[22] J. Zhu, L. Yu, Z. Wang, X. Wang, Y. Ou, M. Cai, Z. Wu, R. Tang, Y. Xia, Y. Wang, H. Deng, *ACS Appl. Mater. Interfaces* **2023**, *15*, 28175.
[23] A. Vishwanathan Vidyanagar, S. V. Bhat, *ACS Appl. Mater. Interfaces* **2024**, *16*, 3631.
[24] Q.-B. Zhu, B. Li, D.-D. Yang, C. Liu, S. Feng, M.-L. Chen, Y. Sun, Y.-N. Tian, X. Su, X.-M. Wang, S. Qiu, Q.-W. Li, X.-M. Li, H.-B. Zeng, H.-M. Cheng, D.-M. Sun, *Nat. Commun.* **2021**, *12*, 1798.
[25] P. Prajapat, P. Vashishtha, D. K. Singh, R. K. Mukherjee, J. Tawale, L. Goswami, G. Gupta, *Sensor. Act. A-Phys.* **2024**, *369*, 115151.
[26] H. Yoo, I. S. Lee, S. Jung, S. M. Rho, B. H. Kang, H. J. Kim, *Adv. Mater.* **2021**, *33*, 2006091.

© 2025 Wiley-VCH GmbH

21951071, 2025, 22, Downloaded from https://advanced.onlinelibrary.wiley.com/doi/10.1002/adom.202501192 by Nanjing University, Wiley Online Library on [04/11/2026]. See the Terms and Conditions (https://onlinelibrary.wiley.com/terms-and-conditions) on Wiley Online Library for rules of use; OA articles are governed by the applicable Creative Commons License

[27] H. Huang, Y. Yang, H. Chen, F. Qin, B. Yu, R. Wang, Q. Cao, T. Wang, Q. Lin, *ACS Appl. Mater. Interfaces* **2022**, *14*, 57419.
[28] Y. Zhang, L. Wang, Y. Lei, B. Wang, Y. Lu, Y. Yao, N. Zhang, D. Lin, Z. Jiang, H. Guo, J. Zhang, H. Hu, *ACS Nano* **2022**, *16*, 20937.
[29] H. Liu, W. Dong, H. Wang, L. Lu, Q. Ruan, Y. S. Tan, R. E. Simpson, J. K. W. Yang, *Sci. Adv.* **2020**, *6*, abb7171.
[30] M. Okil, A. Shaker, I. S. Ahmed, T. M. Abdolkader, M. S. Salem, *Sol. Energy Mater Sol. Cells* **2023**, *253*, 112210.
[31] M. S. Salem, A. Shaker, M. S. Othman, A. H. Al-Bagawia, M. Fedawy, G. M. Aleid, *Opt. Mater.* **2022**, *123*, 111880.
[32] Y. Yin, C. Wu, R. Tang, C. Jiang, G. Jiang, W. Liu, T. Chen, C. Zhu, *Sci. Bull.* **2019**, *64*, 136.
[33] W. Lian, C. Jiang, Y. Yin, R. Tang, G. Li, L. Zhang, B. Che, T. Chen, *Nat. Commun.* **2021**, *12*, 3260.

© 2025 Wiley-VCH GmbH

21951071, 2025, 22, Downloaded from https://advanced.onlinelibrary.wiley.com/doi/10.1002/adom.202501192 by Nanjing University, Wiley Online Library on [04/11/2026]. See the Terms and Conditions (https://onlinelibrary.wiley.com/terms-and-conditions) on Wiley Online Library for rules of use; OA articles are governed by the applicable Creative Commons License